International Journal of Heat and Mass Transfer 149 (2020) 119161

Contents lists available at ScienceDirect

International Journal of Heat and Mass Transfer

journal homepage: www.elsevier.com/locate/hmt

Forced convection in additively manufactured sandwich-walled cylinders with thermo-mechanical multifunctionality

Shanyouming Sun[a,b,c], Shangsheng Feng[c,d,*], Qiancheng Zhang[a], Tian Jian Lu[b,e,**]

[a] State Key Laboratory for Strength and Vibration of Mechanical Structures, Xi'an Jiaotong University, Xi'an 710049, PR China
[b] State Key Laboratory of Mechanics and Control of Mechanical Structures, Nanjing University of Aeronautics and Astronautics, Nanjing 210016, PR China
[c] Bioinspired Engineering and Biomechanics Center (BEBC), Xi'an Jiaotong University, Xi'an 710049, PR China
[d] The Key Laboratory of Biomedical Information Engineering of Ministry of Education, School of Life Science and Technology, Xi'an Jiaotong University, Xi'an 710049, PR China
[e] Nanjing Center for Multifunctional Lightweight Materials and Structures (MLMS), Nanjing University of Aeronautics and Astronautics, Nanjing 210016, PR China

ARTICLE INFO

Article history:
Received 6 September 2019
Revised 27 November 2019
Accepted 2 December 2019
Available online 25 December 2019

Keywords:
Intersection-of-asymptotes theory
3D printing
Forced convection
Sandwich structure
Combustor

ABSTRACT

Forced convective heat transfer in lightweight sandwich-walled cylinders with quadrangle core (I type) and triangle cores (V, N, W and M type) was investigated experimentally, numerically and theoretically, targeting multifunctional applications (*e.g.*, combustion chamber) requiring simultaneous load bearing and heat dissipation. Sandwich-walled cylinder with the N type core was fabricated using 3D-printing technology. Forced convection experiments were carried out to validate numerical simulation results and to reveal varying flow stages in the channels of the sandwich wall. Flow in these channels changed from laminar ($Re < 2200$), transition ($2200 < Re < 4100$) to vigorous turbulence stage ($Re > 4100$) as the Reynolds number was increased. With the total heat dissipation area fixed, the heat transfer performance of the quadrilateral core (I type) was better than triangular cores (V, N, W and M type). Among the triangular cores, those with homogeneous pore structure (V and N) exhibited superior heat transfer performance in comparison with the nonhomogeneous ones (W and M type). The optimal number of unit cells for each core type was determined using the theory of intersection-of-asymptotes. With the unit cell number optimized for each core, the I core exhibited the best heat dissipation performance while the M core had the worst. Under structural loading, however, the buckling resistance of the I core was not as good as the triangular ones. Thermal and mechanical synergy must be considered in the selection of sandwich core topology for multifunctional applications.

1. Introduction

In aerospace, power systems, transportation and other major engineering fields, the main structural components often need to withstand extremely high heat flux and pressure load [1]. For example, it is essential for the combustion chamber of a Pulse Detonation Engine to organize efficient combustion under high temperature and high pressure to convert the chemical energy of fuel into thermal energy. The wall of a rocket engine combustion chamber with a thrust-weight ratio of 10 needs to withstand 1850–1950 K high temperature and 2.5–3.0 MPa high pressure [2]. The increasingly harsh working environment puts forward demanding requirements for materials and structure design. In particular, with traditional laminate structures, it is difficult to meet the multifunctional requirement of simultaneous load bearing, heat dissipation and lightweight. Sandwich structures with high stiffness, lightweight, efficient heat transfer and other multifunctional attributes have great potential in this field [3,4]. Especially, the application of sandwich-walled cylinders in combustion chambers can not only effectively reduce structural weight, but also enable active cooling by fluid convection in the sandwich cores [5].

While multifunctional design of lightweight sandwich structures has been a long-standing research topic [1], the selection and design of a suitable sandwich core is the key to meet the multifunctional requirements. The core structure is versatile and can be individually designed to meet specific requirements [6]. On the other hand, in recent years, the rapid development of metal

* Corresponding author at: Bioinspired Engineering and Biomechanics Center (BEBC), Xi'an Jiaotong University, Xi'an 710049, PR China.
** Corresponding author at: State Key Laboratory of Mechanics and Control of Mechanical Structures, Nanjing University of Aeronautics and Astronautics, Nanjing 210016, PR China.
E-mail addresses: shangshengfeng@xjtu.edu.cn (S. Feng), tjlu@nuaa.edu.cn (T.J. Lu).

https://doi.org/10.1016/j.ijheatmasstransfer.2019.119161
0017-9310/

Nomenclature

R_i	inner radius of sandwich-walled cylinder
R_0	outer radius of sandwich-walled cylinder
t_f	facesheet thickness
t_c	core thickness
L	axial length of sandwich-walled cylinder
n	number of unit cells
S_t	total heat dissipation area
D	hydraulic diameter
h	overall heat transfer coefficient of the sandwich-walled cylinder
$T_{w,in}$	average inner facesheet temperature of sandwich-walled cylinder at entrance
$T_{w,middle}$	average inner facesheet temperature of sandwich-walled cylinder at midpoint
$T_{w,out}$	average inner facesheet temperature of sandwich-walled cylinder at exit
$T_{f,in}$	temperature of cooling air at entrance
$T_{f,out}$	average temperature of cooling air at exit
Nu	Nusselt number
Re	Reynolds number
f	flow friction factor
Δp	pressure difference between inlet and outlet
U	average flow velocity
c_p	specific heat of air
k	thermal conductivity
Pr	Prandtl number
w_A	appointed flow velocity at channel entrance ($w_A=\varepsilon_p U$)
q	heat flux applied on inner facesheet
S	cross-sectional area of duct
C	wet circumference of duct
M	total mass flow rate
P	total pumping power
q_0	equivalent heat flux applied uniformly on wetted surface
$T_{w,L}$	average temperature of channel wall at outlet
ΔT	average temperature rise of channel wall at outlet

Greek Symbols

ε_p	porosity
θ	radian of unit cells
ν	kinematic viscosity of air
ρ	density of air
μ	dynamic viscosity of air
μ_t	turbulent viscous coefficient
Γ_t	turbulent diffusion coefficient
Ψ	flow shape factor of duct
τ_w	average wall shear stress

Subscripts

u	upper duct
d	lower duct
1	Limit I: fully developed case
2	Limit II: boundary layer case

3D-printing technology has facilitated the manufacture of complex cores [7], thus laying a solid foundation for the integrated design of load capacity and heat dissipation for all-metallic sandwich structures.

In the field of mechanical design, the load capacity of a triangular core (such as ripple, diamond, etc.) is better than that of a quadrilateral core (such as I core and the like) having the same mass. This is because deformation of the triangular core is dominated by tension or compression rather than bending for the quadrilateral core [8]. Su et al. [9] designed and manufactured an all-metallic triangular-cored sandwich cylindrical shell, and studied its quasi-static axial compression behavior through experimental measurement, numerical simulation and theoretical modeling. It was demonstrated that sandwich-walled shells with triangular cores had superior energy absorption capacity than monolithic shells. However, under out-of-plane compressive load, the triangular core is prone to elastic-plastic buckling at relatively small strain [10] and, as a consequence, its load capacity decreases rapidly. By adding I-type ribs into the triangular core to construct a hybrid triangular-quadrilateral core, the buckling resistance can be effectively enhanced. The Y-shaped sandwich core, as one of the triangular and quadrilateral hybrid cores, was first proposed to improve the crashworthiness of a ship hull by welding steel plates on the outer side of a corrugated core, which has been proven through full scale tests to have a significantly higher resistance to tearing than the conventional single skin design [11]. Rubino et al. [12] studied the three-point bending behavior of triangular corrugated sandwich beams and Y-shaped core sandwich beams. It was found that the two sandwich structures exhibit equivalent bending performance, and their initial failure strengths under bending load are determined by indentation buckling of the core.

In terms of heat transfer characteristics, the existing literature has mainly focused on the heat transfer and flow resistance characteristics of honeycomb [13], rectangle [14], triangle [3] and other core types [15] in sandwich plate configurations. For example, based on the classical fin approach, Lu [13] evaluated the convective heat transfer performance of honeycomb-cored sandwich panels as heat sink for active cooling of power electronics. Zhao and Lu [14] used both the porous medium model and the fin approach to study the heat transfer performance of microchannel heat sinks (I-type core). Xie et al. [3] analyzed the flow and heat transfer characteristics of an actively cooled thermal protection system with corrugated sandwich plates. Wen et al. [16] used the intersection-of-asymptotes method to optimize the forced convection heat transfer of various two-dimensional cores of all-metallic sandwich panels at fixed pumping power.

Existing heat transfer studies were limited to flat sandwich panels except for the study of Liu et al. [5] and Wang et al. [17] on sandwich-walled cylinders. Although Wen et al. [16] and Liu et al. [5] have both utilized the intersection-of-asymptotes method first proposed by Bejan [18] to study the heat dissipation capacity of sandwich structures, they only considered constant wall temperature boundary condition. Theoretical heat dissipation analysis for sandwich structures under constant heat flux boundary condition is rare. Strictly, in real working environment the exact boundary condition of a combustion chamber wall should be neither constant temperature nor constant heat flux, but in between the two. Existing literature studies showed that the constant heat flux boundary condition is more close to real situation than the constant temperature boundary condition [19,20], as significant temperature gradient exists along the streamwise direction of coolant flow in the combustion chamber. Further, there exists no experimental study on heat transfer and flow resistance of sandwich-walled cylinders [17]. In addition, albeit hybrid cores combining triangular and I-type cores have been demonstrated to possess excellent mechanical attributes such as load capacity and buckling resistance, their heat transfer performance is yet investigated. As a result, the multifunctional design of sandwich-walled cylinders remains elusive.

To address the above-mentioned deficiency, forced convective heat transfer characteristics of sandwich-walled cylinders heated by constant heat flux on the inner wall were considered in the current study, as depicted in Fig. 1. A combined experimental, numerical and theoretical approach was employed. Particular empha-

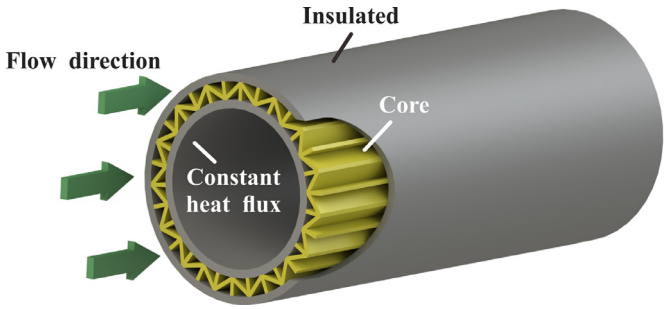

Fig. 1. Schematic of forced convective heat transfer in sandwich-walled cylinder.

sis was placed upon quantifying the influence of pore shape and pore distribution on overall heat transfer and selecting the best core topology for maximal performance.

2. Selection of core topology for sandwich-walled cylinders

The application background of the study is the combustion chamber of a rocket engine, which can be regarded as a typical sandwich-walled cylinder structure with the "I" type of core [20–22]. However, the "I" core is more likely to buckle subjected to compressive loading and its shear strength is weaker compared to the corrugation (V type) core [11,23]. By adding the I-type ribs into the V core, three derived corrugation cores (*i.e.* N, W and M core) were also designed as shown in Fig. 2, which may further improve the mechanical properties of sandwich-walled cylinders. Due to the excellent thermal and mechanical attributes of the five core types (*i.e.* I, V, N, W and M cores), they are potential candidates to be selected as the core of sandwich-walled cylinders for lightweight combustion chambers. In this study, the thermal performance of sandwich-walled cylinders with the five cores were systematically investigated and compared with each other as the first step of the thermo-mechanical multifunctional design.

Key characteristics of the five core types were summarized below, as:

(1) The shape of the unit cell shape for the V, N, W and M core types was triangular, but quadrilateral for the I core.
(2) The N, W and M cores can be regarded as three subtypes derived by adding I ribs at the inner and outer apex angles of the V core.
(3) In terms of structural homogeneity, the pore sizes of the I, V and N cores were uniform along the circumference; whereas the W and M cores had non-uniform pore sizes.

The independent geometric parameters of the proposed sandwich-walled cylinders include: inner radius R_i, outer radius R_0, facesheet thickness t_f, core thickness t_c, radian of circumferential minimum repetitive element θ, and axial length of cylinder L. Among them, θ can be converted from the total number of circumferential maximum repetitive elements n, as $\theta = \pi/n$. The total number of circumferential maximum repetitive units (n) was the main variable in the current study. For convenience of expression, the labeling method of "core type-total number of circumferential maximum repetitive units" was used to refer to a specific sandwich-walled cylinder (*e.g.* "I-61″ refers to the I cored sandwich structure with 61 units).

The derivation process of porosity ε, total heat dissipation area S, and hydraulic diameter D for each core topology was detailed in the Appendix. Explicit expressions of these parameters were listed in Table 1.

3. Forced convective heat transfer experiment

3.1. Sample preparation

To validate the numerical and theoretical models, a sandwich-walled cylinder made of aluminum alloy with inner radius 30 mm, outer radius 40 mm and axial length 100 mm was fabricated using 3D-printing, as displayed in Fig. 3. Specifically, aluminum alloy (AlSi10Mg) powder with particle size 1–50 μm was used to construct the entire structure via powder laying and laser sintering in the 3D printer (Liantai^{TM} 660). The hydraulic diameter of the N-type core channel was 1.6 mm, comparable to the hydraulic diameter of microchannel heat sinks (~ 1 mm) [24]. Table 2 listed the geometric parameters of the printed sample. In this study, the radian of circumferential minimum repetitive element θ was selected as a variable, while the other independent geometric parameters were all fixed. In this study, the radian of circumferential minimum repetitive element θ was selected as a variable, while the other independent geometric parameters were all fixed. It is worth noting that the sample may shrink to a certain extent during the 3D printing process, which was found to be less than 0.18 mm. The final measured sizes of the additively manufactured sample (N-15) were used in the data reduction, which were shown along with the corresponding design values in Table 2.

3.2. Experimental apparatus

As shown in Fig. 4, the experimental system for forced convective heat transfer was composed of seven parts (from left to right): turbine fan, heat exchanger, orifice meter, setting chamber, inlet section, test section and outlet section. The air blown by the turbine fan, after being cooled to room temperature via the heat exchanger, passed through the orifice meter and the setting chamber, then entered into the test sample after the inlet section, and finally discharged into the environment.

In the test section, the sandwich-walled cylinder sample was housed in a sleeve made of resin having the same axial length. Its inner facesheet was bonded with heating pads to provide constant heat flux boundary condition, and insulation foam was wrapped outside the sleeve and filled inside the cylinder to minimize heat loss. To ensure smooth flow at entry/exit of the annular channel of test sample, an annular channel supporting part and a central cylinder rod were designed at the inlet section, as shown in Fig. 4. At the same time, the inner radius of the sleeve was purposely designed to be different from the outer radius of the cylinder by a facesheet thickness, so as to avoid disturbance of flow in the annular channel. Eight T-type thermocouples were evenly embedded in the slots excavated in the inner facesheet, six of which were arranged separately along the circumferential direction at the inlet and outlet to check the uniformity of circumferential temperature. All the thermocouple wires were extended from the inner cavity of the outlet section and connected to the temperature acquisition device (Agilent^{TM} 34970A). To monitor the air temperature and pressure at the entry and exit, several thermocouples and pressure tapping were located in the inlet and outlet sections, respectively. A polymer foam matrix was placed downstream the sample to mix the flow leaving the sample, so that the average air temperature at the exit could be measured.

3.3. Parameters definition

The overall heat transfer coefficient of the present sandwich-walled cylinder was defined as [25]:

$$h = \frac{Q_{in}}{A\left[\left(T_{w,in} + T_{w,middle} + T_{w,out}\right)/3 - T_{f,in}\right]} \tag{1}$$

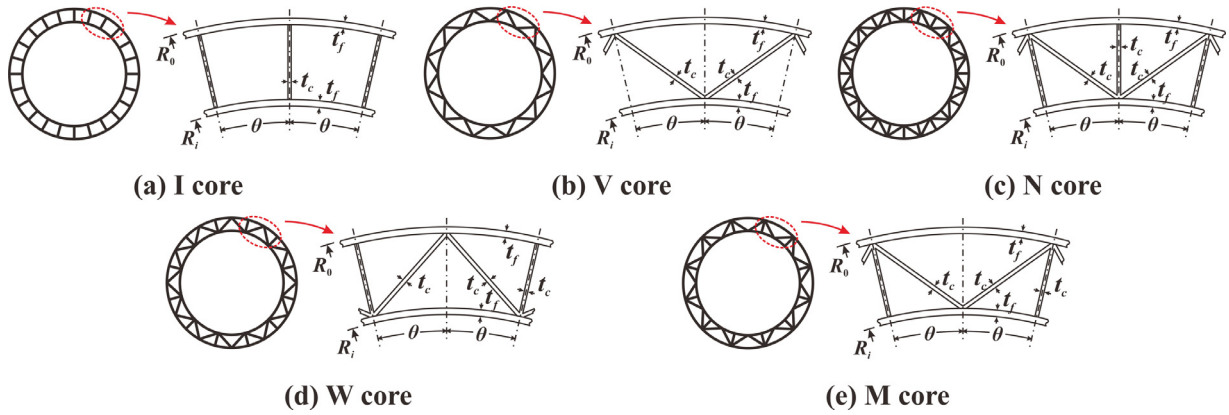

Fig. 2. Schematic of five sandwich-walled cylinders with different core topologies.

Table 1
Geometric parameters of core topologies for sandwich-walled cylinders.

Core type	Unit cell	Porosity ε	Total heat dissipation area S_t	Hydraulic diameter D
I core	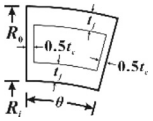	$\frac{2S_{EFGH}}{(R_0^2-R_i^2)\theta}$	$nC_{EFGH}L$	$\frac{4S_{EFGH}}{C_{EFGH}}$
V core	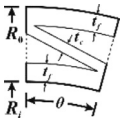	$\frac{2(S_{EFG}+S_{HIJ})}{(R_0^2-R_i^2)\theta}$	$2nC_{GF,IJ,\widehat{EF},\widehat{IH}}L$	$\frac{4(S_{EFG}+S_{HIJ})}{C_{GF,IJ,\widehat{EF},\widehat{IH}}}$
N core	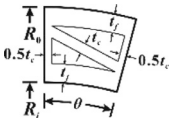	$\frac{2(S_{EFG}+S_{HIJ})}{(R_0^2-R_i^2)\theta}$	$2n(C_{EFG}+C_{HIJ})L$	$\frac{4(S_{EFG}+S_{HIJ})}{C_{EFG}+C_{HIJ}}$
W core	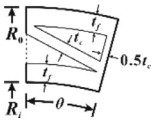	$\frac{2(S_{EFG}+S_{HIJ})}{(R_0^2-R_i^2)\theta}$	$2n(C_{GF,\widehat{EF}}+C_{HIJ})L$	$\frac{4(S_{EFG}+S_{HIJ})}{C_{GF,\widehat{EF}}+C_{HIJ}}$
M core	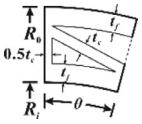	$\frac{2(S_{EFG}+S_{HIJ})}{(R_0^2-R_i^2)\theta}$	$2n(C_{EFG}+C_{\widehat{IJ,IH}})L$	$\frac{4(S_{EFG}+S_{HIJ})}{C_{EFG}+C_{\widehat{IJ,IH}}}$

Table 2
Geometric parameters of sandwich-walled cylinder (N-15) manufactured by 3D-printing.

	Inner radius R_i (mm)	Outer radius R_0 (mm)	Facesheet thickness t_f (mm)	Core thickness t_c (mm)	Axial length L (mm)	Hydraulic diameter D (mm)
Design	15.00	21.50	1.50	0.80	100.00	1.60
Measured	14.91	21.44	1.52	0.82	99.86	1.58

(a) (b)

Fig. 3. Sandwich-walled cylinder manufactured via 3D-printing: (a) holistic view; (b) top view.

where $T_{w,in}$, $T_{w,middle}$ and $T_{w,out}$ were the average temperatures of the inner facesheet at the entrance, the midpoint and the exit, respectively. $T_{f,in}$ was the temperature of cooling air at the entrance (~ 300 K). $T_{f,out}$ was the average temperature of air at the exit. Nusselt number of heat transfer was defined as:

$$\mathrm{Nu} = \frac{hD}{k} \tag{2}$$

The flow friction factor and the Reynolds number were defined as:

$$f = \frac{2\Delta pD}{\rho U^2 L} \tag{3}$$

$$\mathrm{Re} = UD/\nu \tag{4}$$

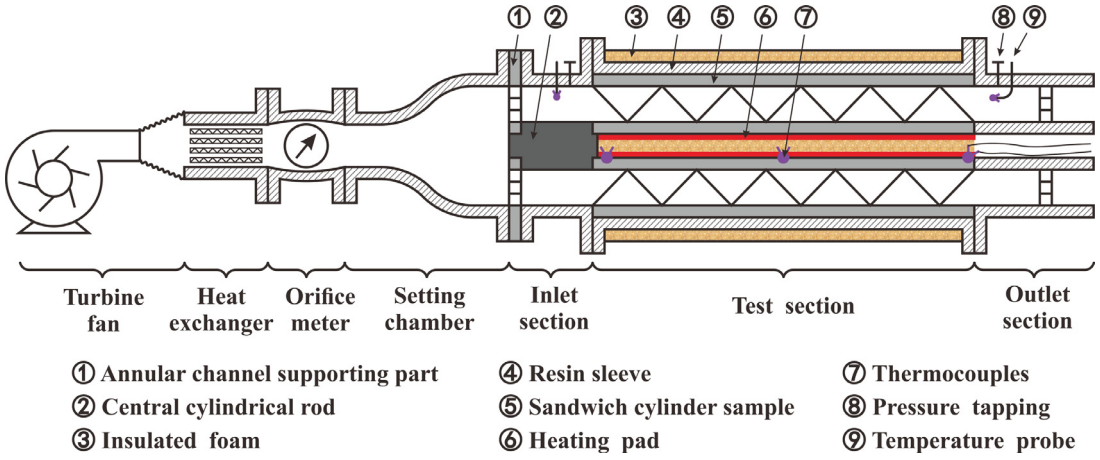

Fig. 4. Schematic of forced convection experimental apparatus.

where Δp was the pressure difference between the inlet and outlet, D was the hydraulic diameter of the sample duct, ν is the kinematic viscosity of air, and U was the average flow velocity in sample duct.

3.4. Uncertainty analysis

To calculate the uncertainty of combined variables, it is necessary to determine the uncertainty of direct measurements such as pressure, temperature and length. Experimental error sources in the study included three aspects: thermal power measurement, thermocouple reading and geometric measurement [26,27]. According to Kline and McClintock [28], the uncertainty of heat transfer coefficient and the flow friction factor defined by (1) and (3) can be calculated respectively as:

$$\frac{\delta h}{h}=\sqrt{\left(\frac{\delta Q_{in}}{Q_{in}}\right)^2+\left(\frac{\delta A}{A}\right)^2+\frac{1}{9}\cdot\frac{(\delta T_{w,in})^2+\left(\delta T_{w,middle}\right)^2+(\delta T_{w,out})^2}{\left[\left(T_{w,in}+T_{w,middle}+T_{w,out}\right)/3-T_{f,in}\right]^2}+\left[\frac{\delta T_{f,in}}{\left(T_{w,in}+T_{w,middle}+T_{w,out}\right)/3-T_{f,in}}\right]^2} \tag{5}$$

$$\frac{\delta f}{f}=\sqrt{\left(\frac{\delta\Delta p}{\Delta p}\right)^2+\left(\frac{2\delta M}{M}\right)^2+\left(\frac{\delta D}{D}\right)^2+\left(\frac{\delta L}{L}\right)^2+\left(\frac{2\delta S}{S}\right)^2} \tag{6}$$

The error of voltage and current supplied by DC power supply was 0.5%, so the error of thermal power input was 1.5%. The measurement error of facesheet area A was about 1%. The reading error of thermocouples was 0.3 °C. Typical temperature difference in the experiments was about 30 K, so the error of temperature measurements was 1%. Based on the above values, the error of heat transfer coefficient was evaluated to be 2.14% according to (5).

The typical pressure difference Δp during the experiment was in the order of 100 Pa, and its measurement uncertainty was about 1 Pa, so its error was estimated to be 1%. The mass flow rate M during the experiment was on the order of 1×10^{-3} kg/s, while its measurement uncertainty was about 1×10^{-6} kg/s, so its error was 1%. The geometric measurement errors of hydraulic diameter D, axial length L and cross-sectional area of duct S were 0.5%, 1% and 2% respectively. Based on the above values, the error of flow friction factor was evaluated to be 3.32% according to (6).

4. Numerical simulation

4.1. Computational domain, governing equations and boundary conditions

The sandwich-walled cylinder was made of aluminum alloy, and the cooling fluid was dry air at room temperature (300 K). The annular flow region was divided into independent straight ducts by cores having different cross-sectional shapes. Due to periodicity and symmetry along the circumferential direction of the cylinder, the computational domain was chosen as an annular minimum repeating unit, as shown in Fig. 5.

Experimental observations of Eckert and Irvine [29] revealed that the transition from laminar to turbulent flow happens at $Re = 1000$ for a duct with triangular cross-section of an apex angle of 11.5°. For V-shaped finned internally tube with 20 unit cells, it was also found [30] that flow transition occurs at about $Re = 600$.

The Reynolds number in the current study has been tested in the range of 100–5000, which may cover laminar, transitional and turbulent flow regions. Therefore, the numerical simulations applied both the laminar flow model and the k-ε turbulence model, and the calculation results of the two models were compared with experimental measurements. Other assumptions adopted for performing the numerical simulation included:

(1) The flow was three-dimensional, incompressible and steady with no viscous dissipation;
(2) Thermal properties of fluid and solid were constant;

Based on these assumptions, the governing equations of the numerical model were [31]:

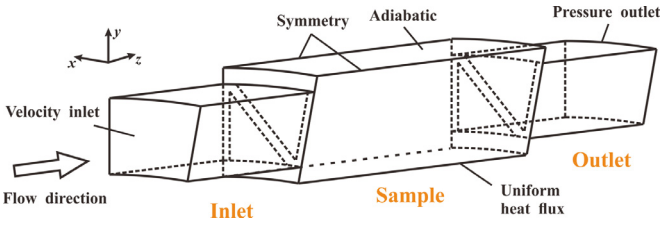

Fig. 5. Computational domain for forced convection in sandwich-walled cylinder.

Table 3
Thermal properties adopted in numerical simulation.

	Density ρ (kg•m^{-3})	Specific heat c_p (J•kg^{-1}•K^{-1})	Dynamic viscosity μ (Pa•s)	Thermal conductivity k (W•m^{-1}•K)
Air	1.225	1006.43	1.7894×10^{-5}	0.0242
Aluminum alloy	–	–	–	110

Continuity equation:

$$\frac{\partial u_j}{\partial x_j} = 0 \tag{7}$$

Momentum equations:

$$\frac{\partial}{\partial x_j}(\rho u_i u_j) = -\frac{\partial p}{\partial x_i} + \frac{\partial}{\partial x_j}\left(\mu\frac{\partial u_i}{\partial x_j} - \rho\overline{u'_i u'_j}\right)(i = 1, 2, 3) \tag{8}$$

Energy equation:

$$\frac{\partial}{\partial x_j}(\rho u_j T) = \frac{\partial}{\partial x_j}\left(\frac{k}{c_p}\frac{\partial T}{\partial x_j} - \rho\overline{u'_j T'}\right) \tag{9}$$

where ρ, c_p, μ and k were the density, specific heat, dynamic viscosity and thermal conductivity of air, respectively. Relevant values were listed in Table 3.

The Reynolds-averaging equations were employed to deal with turbulence, where $\rho\overline{u'_i u'_j}$ was the Reynolds stress generated by instantaneous pulsating flow, and $\rho\overline{u'_j T'}$ was the additional term of turbulence pulsation of temperature. The Reynolds stress was related to the average velocity gradient using vortex viscosity coefficient according to the Boussinesq hypothesis, as:

$$-\rho\overline{u'_i u'_j} = \tau_{ij} = \mu_t\left(2S_{ij} - \frac{2}{3}\frac{\partial u_i}{\partial x_i}\delta_{ij}\right) - \frac{2}{3}\rho k\delta_{ij} \tag{10}$$

where S_{ij} was the strain rate tensor satisfying:

$$S_{ij} = \frac{1}{2}\left(\frac{\partial u_i}{\partial x_j} + \frac{\partial u_j}{\partial x_i}\right) \tag{11}$$

The temperature transmitted by turbulence pulsation was related to the time-averaging parameters via:

$$-\rho\overline{u'_j T'} = \Gamma_t\frac{\partial T}{\partial x_j} \tag{12}$$

In the above equations, μ_t was the turbulent viscous coefficient, and Γ_t was the turbulent diffusion coefficient.

The standard k-ε turbulent model was chosen to evaluate the turbulent viscous coefficient, as:

Turbulent kinetic energy equation*:*

$$\rho\frac{\partial k}{\partial t} + \rho u_j\frac{\partial k}{\partial x_j} = \frac{\partial}{\partial x_j}\left[\left(\mu + \frac{\mu_t}{\sigma_k}\right)\frac{\partial k}{\partial x_j}\right] + \mu_t\frac{\partial u_i}{\partial x_j}\left(\frac{\partial u_i}{\partial x_j} + \frac{\partial u_j}{\partial x_i}\right) - \rho\varepsilon \tag{13}$$

Turbulence dissipation *equation:*

$$\rho u_k\frac{\partial \varepsilon}{\partial x_k} = \frac{\partial}{\partial x_j}\left[\left(\mu + \frac{\mu_t}{\sigma_\varepsilon}\right)\frac{\partial \varepsilon}{\partial x_k}\right] + \frac{c_1\varepsilon}{k}\mu_t\frac{\partial u_i}{\partial x_j}\left(\frac{\partial u_i}{\partial x_j} + \frac{\partial u_j}{\partial x_i}\right) - c_2\rho\frac{\varepsilon^2}{k} \tag{14}$$

The turbulence viscosity and turbulent diffusion coefficient could then be evaluated as:

$$\mu_t = \rho c_\mu\frac{k^2}{\varepsilon} \tag{15}$$

$$\Gamma_t = \frac{\mu}{\mathrm{Pr}} + \frac{\mu_t}{\sigma_t} \tag{16}$$

where σ_t was the turbulent Pr number related to the temperature field, μ/Pr was caused by molecular diffusion, while μ_t/σ_t was due to turbulent fluctuation. The model coefficients and constants selected were: c_1=1.44, c_2=1.92, c_μ=0.09, σ_k=1.0, σ_ε=1.3, σ_t=0.95.

Velocity and pressure boundary conditions were applied to the inlet and outlet of the computational domain, respectively, while symmetry boundary condition was applied to the two sides. The bottom was heated by uniform heat flux, and the remaining solid walls were non-slip and thermally adiabatic. The above boundary conditions can be mathematically described as:

Inlet:

$$w = w_A, T_{in} = 300K \tag{17}$$

Outlet:

$$p = 0, \frac{\partial T}{\partial z} = 0, T_{backflow} = 300K \tag{18}$$

Two sides:

$$\frac{\partial u}{\partial n} = \frac{\partial v}{\partial n} = \frac{\partial w}{\partial n} = \frac{\partial T}{\partial n} = 0 \tag{19}$$

Bottom:

$$q = -k\frac{\partial T}{\partial n} \tag{20}$$

Solid walls at the top and inlet/outlet:

$$u = v = w = 0, q = 0 \tag{21}$$

where w_A was the appointed flow velocity at the channel entrance (w_A=$\varepsilon_p U$), and q was the uniform heat flux applied to the inner facesheet.

The boundary conditions at solid/fluid interfaces did not need to be specified since the momentum and energy equations were automatically coupled to ensure the continuity of velocity, stress, temperature and heat flux at these interfaces.

4.2. Numerical methods

A multi-block structured mesh incorporating fully hexahedral elements was generated by Gambit 2.4.6 in all fluid and solid domains. A commercial CFD code (ANSYS Fluent 14.5) was used to solve the current problem [32]. The SIMPLE algorithm was applied to couple the pressure and velocity for numerical analysis [33,34]. A second-order upwind scheme was applied to discretize the convective terms in the governing equations. The iterative convergence criterion was chosen as 10^{-3} for momentum equation and 10^{-6} for energy equation. For selected cases, these were verified to be small enough to ensure the numerical results independent of the selected values. To check the grid dependency, the number of elements was increased from 0.4 million to 2 million: for both cases, the calculation results showed no difference.

5. Theoretical model of intersection-of-asymptotes for heat transfer optimization

To optimize core structure parameters, a theoretical model to maximize the heat transfer in sandwich-walled cylinder was established. To this end, as shown schematically in Fig. 6, the inner facesheet was heated by constant heat flux q, and the outer

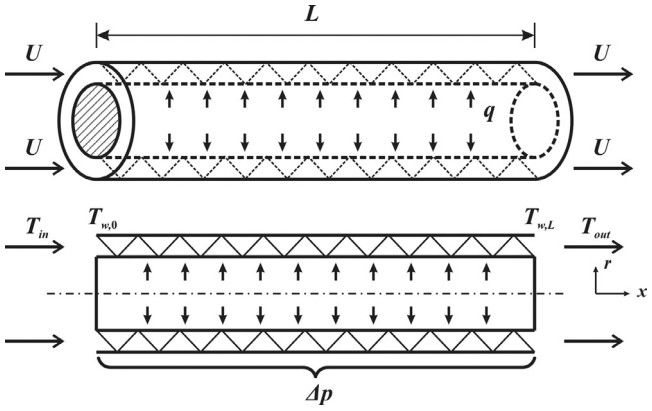

Fig. 6. Pressure drop and heat transfer in sandwich-walled cylinder: theoretical modeling.

facesheet was adiabatic. The pressure difference between the inlet and outlet was Δp through the sample of length L, and the pressure at the inlet and outlet was assumed to be uniform. Therefore, the flow velocities in different ducts (the upper and lower ducts marked as u and d, respectively) of V, N, W or M cores were unequal as the flow resistance was dependent upon core topology. If U was the average velocity in a channel, S was the cross-sectional area and C was the wet circumference of the duct, the total mass flow rate M and the total pumping power P could be expressed as:

$$M=2n\rho(U_dS_d+U_uS_u) \tag{22}$$

$$P=2n\Delta p(U_dS_d+U_uS_u) \tag{23}$$

where n was the total number of core units along the circumference.

Since the thermal conductivity of metal is much larger than that of air, the heat flux (q) on the inner facesheet could be assumed to be uniformly applied on the wetted surfaces in each channel (q_0). Heat flux on the wetted surfaces of each channel could thus be calculated as:

$$q_0=\frac{\pi R_i}{n(C_u+C_d)}q \tag{24}$$

Next, for each core type, theoretical expressions of heat transfer and flow resistance of the sandwich-walled cylinder were deduced under two extreme conditions: (I) fully developed case and (II) boundary layer case. Through asymptotic intersection of the two extreme conditions, optimal structural parameters for each core type were obtained. Given the constant heat flux boundary condition, the objective of optimization was to minimize the temperature rise of inner facesheet at the outlet, subjected to the constraint of fixed pressure drop or pumping power.

5.1. Limit I: fully developed case

5.1.1. Flow resistance

Consider first the fully developed flow and heat transfer, which means $L\to\infty$, or equivalently, the hydraulic diameter of the channel $D\to 0$. In this case, each duct became sufficiently slender, and the pressure drop (Δp) across the duct could be calculated as:

$$f\cdot \mathrm{Re}=64\Psi \tag{25}$$

where Ψ was the flow shape factor of the duct [35]; f, Re were the friction factor and Reynolds number, respectively, as defined in Eqs. (3) and (4). Combining the above equations led to:

$$U=\frac{\Delta pD^2}{32\rho L\nu\Psi} \tag{26}$$

Substitution of (26) into (22) and (23) yielded:

$$M=\frac{n\Delta p}{16L\nu}\left(\frac{D_d^2S_d}{\Psi_d}+\frac{D_u^2S_u}{\Psi_u}\right) \tag{27}$$

$$P=\frac{n\Delta p^2}{16\rho L\nu}\left(\frac{D_d^2S_d}{\Psi_d}+\frac{D_u^2S_u}{\Psi_u}\right) \tag{28}$$

Upon combining and solving Eqs. (26), and –(28), the average velocities of each channel were separately expressed as functions of Δp, M and P, as:

fixed pressure drop:

$$U_u=0.03125\rho^{-1}L^{-1}\nu^{-1}\Psi_u^{-1}D_u^2\Delta p \tag{29}$$

$$U_d=0.03125\rho^{-1}L^{-1}\nu^{-1}\Psi_d^{-1}D_d^2\Delta p \tag{30}$$

fixed mass flow rate:

$$U_u=0.5\rho^{-1}n^{-1}\Psi_u^{-1}\left(D_d^2S_d\Psi_d^{-1}+D_u^2S_u\Psi_u^{-1}\right)^{-1}D_u^2M \tag{31}$$

$$U_d=0.5\rho^{-1}n^{-1}\Psi_d^{-1}\left(D_d^2S_d\Psi_d^{-1}+D_u^2S_u\Psi_u^{-1}\right)^{-1}D_d^2M \tag{32}$$

fixed pumping power:

$$U_u=0.125n^{-0.5}\rho^{-0.5}L^{-0.5}\nu^{-0.5}\left(D_d^2S_d\Psi_d^{-1}+D_u^2S_u\Psi_u^{-1}\right)^{-0.5}D_u^2\Psi_u^{-1}P^{0.5} \tag{33}$$

$$U_d=0.125n^{-0.5}\rho^{-0.5}L^{-0.5}\nu^{-0.5}\left(D_d^2S_d\Psi_d^{-1}+D_u^2S_u\Psi_u^{-1}\right)^{-0.5}D_d^2\Psi_d^{-1}P^{0.5} \tag{34}$$

5.1.2. Heat transfer

Let the average temperature of fluid at the outlet of the channel be $T_{f,out}$, and the average wall temperature at the outlet be $T_{w,L}$. Energy conservation dictated:

$$\begin{cases} q_0C_dL=\rho c_pU_dS_d\left(T_{f,out,d}-T_{f,in}\right) \\ q_0C_uL=\rho c_pU_uS_u\left(T_{f,out,u}-T_{f,in}\right) \end{cases} \tag{35}$$

For fully developed flow in a straight channel, Nu is constant [18], namely:

$$\begin{cases} \frac{q_0}{T_{w,L,d}-T_{f,out,d}}\cdot\frac{D_d}{k}=\mathrm{Nu}_d \\ \frac{q_0}{T_{w,L,u}-T_{f,out,u}}\cdot\frac{D_u}{k}=\mathrm{Nu}_u \end{cases} \tag{36}$$

where Nu_u and Nu_d are Nusselt numbers of upper and lower ducts, which could be determined according to the shape of the duct [35]. Combining (29-36), one could obtain the average temperature rise of channel wall at the outlet ΔT_1 ($\Delta T_1=(T_{w,L,u}-T_{f,in}+T_{w,L,d}-T_{f,in})/2$, subscript 1 represents Limit I) in the fully developed case for fixed pressure drop, fixed mass flow rate, or fixed pumping power, as:

fixed pressure drop:

$$\Delta T_1=q_0L\left[128L\nu c_p^{-1}\Delta p^{-1}\left(\Psi_dD_d^{-3}+\Psi_uD_u^{-3}\right)+k^{-1}L^{-1}\left(D_d\mathrm{Nu}_d^{-1}+D_u\mathrm{Nu}_u^{-1}\right)\right] \tag{37}$$

fixed mass flow rate:

$$\Delta T_1=q_0L\left[8nc_p^{-1}M^{-1}\left(D_d^2S_d\Psi_d^{-1}+D_u^2S_u\Psi_u^{-1}\right)\left(\Psi_dD_d^{-3}+\Psi_uD_u^{-3}\right)+k^{-1}L^{-1}\left(D_d\mathrm{Nu}_d^{-1}+D_u\mathrm{Nu}_u^{-1}\right)\right] \tag{38}$$

fixed pumping power:

$$\Delta T_1=q_0L\left[32n^{0.5}\rho^{-0.5}c_p^{-1}L^{0.5}\nu^{0.5}P^{-0.5}\left(D_d^2S_d\Psi_d^{-1}+D_u^2S_u\Psi_u^{-1}\right)^{0.5}\left(\Psi_dD_d^{-3}+\Psi_uD_u^{-3}\right)+k^{-1}L^{-1}\left(D_d\mathrm{Nu}_d^{-1}+D_u\mathrm{Nu}_u^{-1}\right)\right] \tag{39}$$

5.2. Limit II: boundary layer case

This case implies $L\to 0$, or equivalently, the hydraulic diameter of the channel $D\to\infty$. The flow in a single channel was in the state of boundary layer flow: only near the solid wall the velocity and temperature would vary; outside the boundary layer, the flow was non-viscous free flow, independent of friction and heating of the solid wall. Under this extreme condition, the solutions of boundary layer flow could be used to approximate the flow and heat transfer of sandwich-walled cylinder.

5.2.1. Flow resistance

Balance of pressure and friction led to:

$$CL\tau_w = S\Delta p \tag{40}$$

The average wall shear stress τ_w could be obtained from the solution of boundary layer flow of a flat plate [18], as:

$$2\tau_w/\left(\rho U^2\right) = 1.328\mathrm{Re}_L^{-0.5} \tag{41}$$

$$\mathrm{Re}_L = UL/\nu \tag{42}$$

Upon rearranging (40)-(42) and considering the definition of hydraulic diameter ($D = 4S/C$), the average flow velocities through the upper and lower ducts of the core unit cell were derived as functions of pressure drop:

$$U_d = 0.5214D_d^{\frac{2}{3}}\Delta p^{\frac{2}{3}}\rho^{-\frac{2}{3}}\nu^{-\frac{1}{3}}L^{-\frac{1}{3}} \tag{43}$$

$$U_u = 0.5214D_u^{\frac{2}{3}}\Delta p^{\frac{2}{3}}\rho^{-\frac{2}{3}}\nu^{-\frac{1}{3}}L^{-\frac{1}{3}} \tag{44}$$

Upon substituting (43) and (44) into (22) and (23), the average velocity of each duct was obtained for:

fixed mass flow:

$$U_d = 0.5Mn^{-1}\rho^{-1}D_d^{\frac{2}{3}}\left(D_d^{\frac{2}{3}}S_d + D_u^{\frac{2}{3}}S_u\right)^{-1} \tag{45}$$

$$U_u = 0.5Mn^{-1}\rho^{-1}D_u^{\frac{2}{3}}\left(D_d^{\frac{2}{3}}S_d + D_u^{\frac{2}{3}}S_u\right)^{-1} \tag{46}$$

fixed pumping power:

$$U_d = 0.5127P^{\frac{2}{5}}n^{-\frac{2}{5}}\rho^{-\frac{2}{5}}\nu^{-\frac{1}{5}}L^{-\frac{1}{5}}\left(D_d^{\frac{2}{3}}S_d + D_u^{\frac{2}{3}}S_u\right)^{-\frac{2}{5}}D_d^{\frac{2}{3}} \tag{47}$$

$$U_u = 0.5127P^{\frac{2}{5}}n^{-\frac{2}{5}}\rho^{-\frac{2}{5}}\nu^{-\frac{1}{5}}L^{-\frac{1}{5}}\left(D_d^{\frac{2}{3}}S_d + D_u^{\frac{2}{3}}S_u\right)^{-\frac{2}{5}}D_u^{\frac{2}{3}} \tag{48}$$

5.2.2. Heat transfer

Under uniform heat flux, the solution of external flow along a flat plate was [18]:

$$\mathrm{Nu}_x = \frac{q}{T_{w,x} - T_{f,in}}\cdot\frac{x}{k} = 0.453\mathrm{Pr}^{\frac{1}{3}}\mathrm{Re}_x^{\frac{1}{2}} \qquad (0.5 < \mathrm{Pr} < 10) \tag{49}$$

Temperature rise of channel wall at the outlet of upper and lower channels in each unit needed to satisfy:

$$\begin{cases} T_{w,L,d} - T_{f,in} = 2.208q_0k^{-1}\mathrm{Pr}^{-\frac{1}{3}}U_d^{-\frac{1}{2}}L^{\frac{1}{2}}\nu^{\frac{1}{2}} \\ T_{w,L,u} - T_{f,in} = 2.208q_0k^{-1}\mathrm{Pr}^{-\frac{1}{3}}U_u^{-\frac{1}{2}}L^{\frac{1}{2}}\nu^{\frac{1}{2}} \end{cases} \tag{50}$$

Substituting (50) into (43)-(48) led to the wall temperature rise ΔT_2 (ΔT_2=($T_{w,L,u}$-$T_{f,in}$+$T_{w,L,d}$-$T_{f,in}$)/2, subscript 2 represents Limit II) at the outlet of each channel, as:

fixed pressure drop:

$$\Delta T_2 = 3.057q_0L^{\frac{2}{3}}\nu^{\frac{2}{3}}k^{-1}\mathrm{Pr}^{-\frac{1}{3}}\Delta p^{-\frac{1}{3}}\rho^{\frac{1}{3}}\left(D_d^{-\frac{1}{3}} + D_u^{-\frac{1}{3}}\right) \tag{51}$$

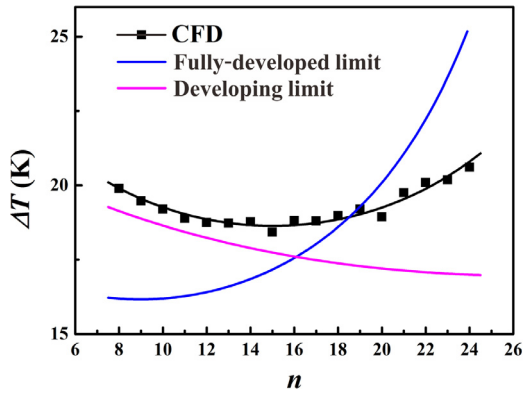

Fig. 7. CFD validation of intersection-of-asymptotes model with fixed pumping power of $P = 3$ W.

fixed mass flow rate:

$$\Delta T_2 = 3.122q_0L^{\frac{1}{2}}\nu^{\frac{1}{2}}k^{-1}\mathrm{Pr}^{-\frac{1}{3}}M^{-\frac{1}{2}}n^{\frac{1}{2}}\rho^{\frac{1}{2}}\left(D_d^{\frac{2}{3}}S_d + D_u^{\frac{2}{3}}S_u\right)^{\frac{1}{2}}\left(D_d^{-\frac{1}{3}} + D_u^{-\frac{1}{3}}\right) \tag{52}$$

fixed pumping power:

$$\Delta T_2 = 3.083q_0L^{\frac{3}{5}}\nu^{\frac{3}{5}}k^{-1}\mathrm{Pr}^{-\frac{1}{3}}\widehat{P}^{-\frac{1}{5}}n^{\frac{1}{5}}\rho^{\frac{1}{5}}\left(D_d^{\frac{2}{3}}S_d + D_u^{\frac{2}{3}}S_u\right)^{\frac{1}{5}}\left(D_d^{-\frac{1}{3}} + D_u^{-\frac{1}{3}}\right) \tag{53}$$

5.3. Validation of the intersection-of-asymptotes model

For a single-layer core as shown in Fig. 2, take the condition of fixed pumping power as an example. In the limit I of fully developed case ($D\to 0$), Eq. (39) showed $\Delta T\sim D^{-2}$, implying that the thermal resistance decreased with increasing D at the power of 2. In the limit case II of the boundary layer case, however, it followed from Eq. (53) that $\Delta T\sim D^{-1/5}$: that is, the thermal resistance decreased with the increase of D at the power of 1/5. Therefore, the speed of change in thermal resistance dramatically changed from limit I to limit II. As a consequence, by employing the intersection-of-asymptotes model, optimal core structure parameters could be obtained at the intersection of heat transfer curves (*i.e.*, $\Delta T_1 = \Delta T_2$) of the two extreme conditions.

For illustration, consider core type N. Let the inner and outer radii of the cylinder, the thickness of facesheet, and the height of core be all fixed. The optimal unit number n (*i.e.*, the optimal heat dissipation area) was obtained under the fixed pumping power condition. To validate the theoretical model prediction, CFD simulations with the laminar flow model (which will be validated in the next section) were carried out and results from the two approaches were compared with each other. As shown in Fig. 7, when the pumping power was fixed at 3 W, in the fully developed case the overall heat transfer coefficient increased with increasing unit number n, while in the boundary layer case the overall heat transfer coefficient decreased with n. Therefore, to maximize the overall heat transfer efficiency, there must exist an optimal n, which occurs at the intersection point of the two asymptotes. The numerical results also verified the theoretical model: the overall heat transfer coefficient increased first and then decreased as the unit number was increased, and the optimal number of core units was around 16 in the example considered.

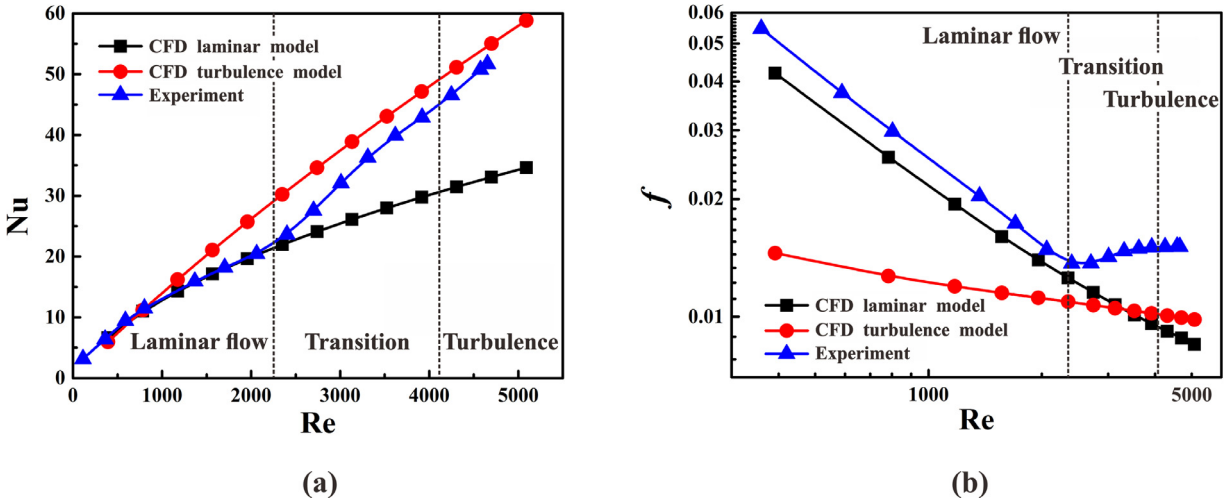

Fig. 8. Comparison between experimental and numerical results for (a) heat transfer and (b) flow resistance for the N-15 sample.

6. Results and discussion

6.1. Analysis of laminar, transitional and turbulent flow in sandwich-walled cylinder

The flow state in a sandwich-walled cylinder is influenced by many factors such as the Reynolds number, the pore morphology and the wall thickness. For a given core morphology, the flow state may change from laminar, transition and turbulent flow successively as increasing the Reynolds number. Based on CFD and experimental results, flow state in the core of test sample N-15 was analyzed. The Nu-*Re* and *f*-*Re* curves obtained from experiments and simulations were displayed in Figs. 8(a) and (b), respectively. To identify the flow stage, both the laminar and turbulent simulation results were presented and compared with experimental results. The *k*-ε turbulence model with standard wall function was used in turbulence simulation, applicable in the fully turbulent flow region. The results of Fig. 8 showed that the flow state in the N-15 sample could be divided into three regions according to the Reynolds number, as elucidated below.

(1) *In the laminar flow region (Re < 2200)*, the friction factor decreased linearly as the Reynolds number was increased, and the Nusselt number increased with increasing Reynolds number but the rate of increase was lower than that in the transitional or fully turbulent regime. The experimental results fairly revealed these typical features, and the laminar flow model predictions agreed better with the experimental results than the turbulent model in the laminar flow region.

(2) *In the transitional flow region (2200 < Re < 4100)*, the flow began to be unstable, and small disturbances in the boundary layer would affect the mainstream flow. Transitions could be clearly observed from both the Nu-*Re* and *f*-*Re* curves. Due to the complicated chaotic and unsteady flow nature, both the steady laminar CFD model and the *k*-ε turbulence model failed to predict the experimental results well in the transitional flow region.

(3) *In the vigorous turbulent flow region (Re > 4100)*, the friction factor became constant after a sharp decrease and transition in the laminar and transitional regimes. Compared to the laminar model, the *k*-ε turbulence model predicted the trend more accurately; although the experimentally measured friction factor was higher than that predicted by the turbulent model, which might be caused by the roughness of the sample made via 3D-printing. Further, in terms of heat transfer, the *k*-ε turbulence model was again much more accurate than the laminar model relative to the experimental results in the vigorous turbulent flow region.

Carlson and Irvine [36] investigated the friction resistance of air flow in isosceles triangular ducts. The results showed that the Reynolds numbers at the beginning of flow transition in different ducts with the apex angles ranging from 4.01 to 38.8° were about 2000, which is similar to the critical Reynolds number (~2200) in the channel of present triangular-cored sandwich-walled cylinder.

It should be pointed out that, due to the complexity of flow transition and turbulence in the sandwich-walled cylinder, the thermal performance of the sandwich-walled cylinders was concerned only in the laminar flow region in the study. Therefore, in other sections of the paper, the CFD results are all based on the laminar CFD model.

6.2. Effect of core morphology on heat transfer and flow resistance

In this section, the effect of core morphology on heat transfer and flow resistance was investigated in the laminar flow region using the laminar numerical model. Fig. 9 presented the heat transfer and flow resistance curves of the five core types having identical total surface area: I-61, V-35, N-15, W-22 and M-26. It was seen that for the cores with homogeneous structure (*i.e.*, uniform pore size such as I-61, V-35 and N-15), core morphology significantly affected heat dissipation. For example, the Nusselt number and flow resistance of triangular cores (V-35 and N-15) were almost the same for a given Reynolds number, while the heat transfer capacity of quadrilateral core (I-61) was 5%–20% higher than the triangular cores: this advantage gradually increased as the Reynolds number was increased. Nonetheless, the flow resistance of quadrilateral core was 10% higher than that of triangular cores at the same Reynolds number.

For the V, W and M cores having the same triangular cells, structural non-homogeneity (*i.e.*, non-uniform pore size) also affected heat dissipation. Specifically, the V core was homogeneous while the W and M cores were non-homogeneous. Further, as the inner triangle of the M core was smaller and its outer triangle was larger, its non-uniformity was larger than the W core. Take the V-35, W-22 and M-26 as an example, which had triangular cores and identical heat dissipation area but were different in structural homogeneity. As shown in Fig. 9, with the Reynolds number fixed, the three cores exhibited approximately the same flow resistance, but their heat transfer capacity varied by about 10%. The Nus-

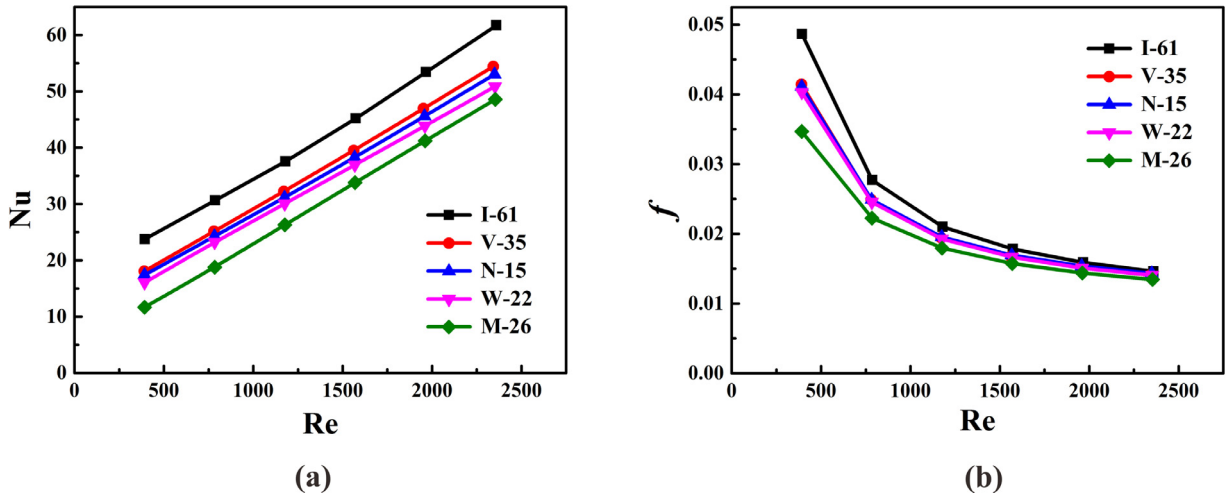

Fig. 9. Comparison of five sandwich cores with different pore shapes but the same total surface area: (a) heat transfer and (b) flow resistance.

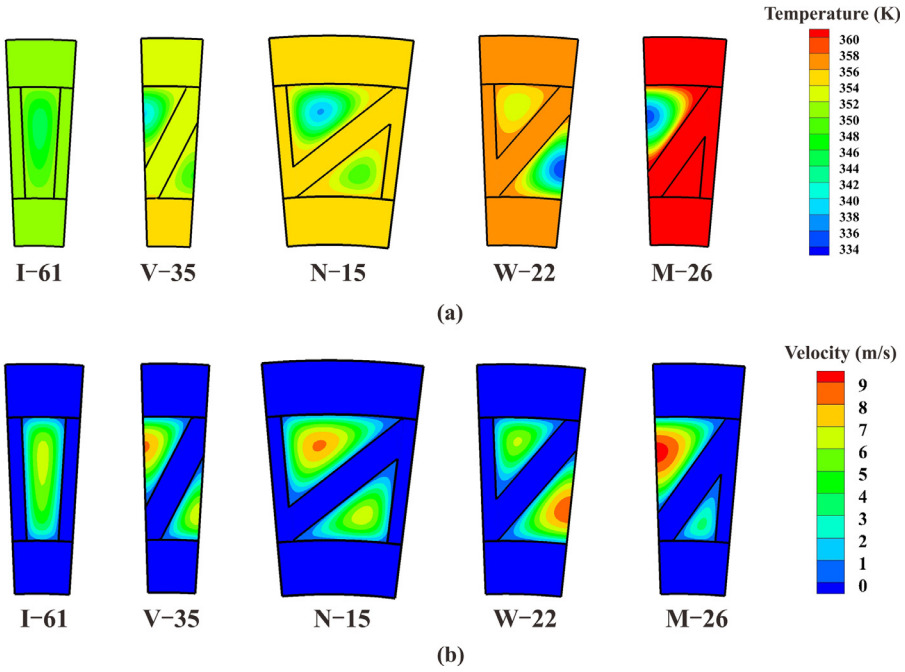

Fig. 10. Temperature and velocity fields at the outlet (z = 100 mm) of different cores with identical heat dissipation area: (a) temperature; (b) velocity.

selt number of V-35 was higher than W-22 and M-26, with M-26 showing the worst heat transfer performance. It might be concluded that, with the same pore shape and the same total surface area, a sandwich core with homogeneous pore morphology could enhance the heat dissipation without increasing the flow resistance at the same Reynolds number.

The present results also revealed that the influence of pore shape was more obvious than pore homogeneity. For example, the quadrilateral core (I core) had the best heat transfer performance, whose Nusselt number and flow resistance were 15% and 10% higher than the triangular cores (V and N), respectively. However, for cores having identical pore shape but different structural homogeneities, the deviation in heat transfer was only up to 10% and structural homogeneity had negligible influence on flow resistance.

The distinct influence of core morphology on heat transfer could be explained from temperature and velocity distributions in the sandwich structures. As shown in Fig. 10, both the velocity and temperature were distributed more non-uniformly in the whole flow channel of the M core compared to other core types, because the cell wall divides the cross-section of the M core into two triangles of different areas. This distribution behavior implied that the main fluid stream flowed through the central region of the channel, with limited flow nearby channel wall. As a result, the thickness of boundary layer nearby the wall of M core was greater than the other core types, which would weaken the mixing of cold and hot fluids, degrade heat transfer efficiency along cell walls, and thus increase the wall temperature. On the contrary, for the I core with open and wide flow channels, the velocity and temperature distributions were more uniform across the whole channel, enabling it to achieve the highest heat transfer efficiency under the constraint of equal total surface area.

6.3. Optimum cell number of the sandwich core

In this section, the optimum cell number of each sandwich core topology was determined at fixed pumping power. The best sand-

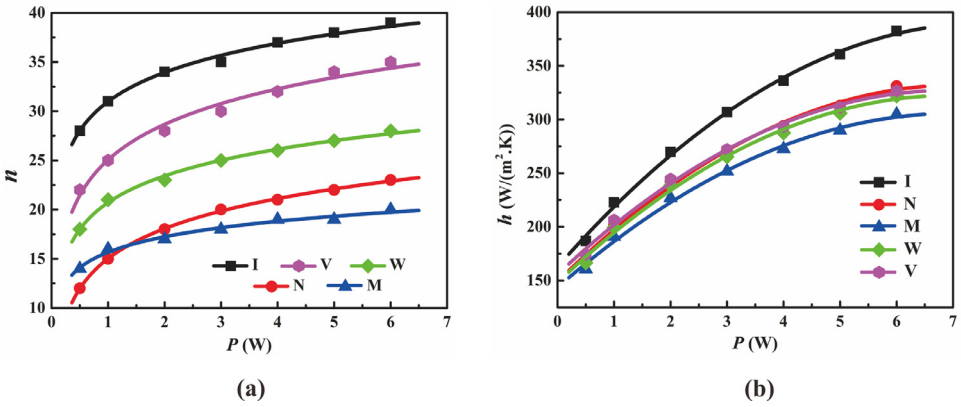

Fig. 11. Optimization of unit cell number for each core type and corresponding maximal heat transfer performance: (a) optimal unit cell number plotted as a function of pumping power; (b) comparison of maximal heat transfer coefficients among 5 core topologies, each having optimal unit cell number.

wich core among the five selected topologies can then be determined by comparing their maximum heat dissipation rates at the corresponding optimum cell numbers. Firstly, the intersection-of-asymptotes model, detailed and validated in Section 5, was used to calculate the optimum number of unit cells for each core type under different pumping powers. From the results presented in Fig. 11(a), it was seen that the optimum number of unit cells increased with pumping power. Secondly, because the theoretical model could not predict the actual heat transfer coefficient but only the optimum number of unit cells, the CFD model was adopted to calculate the actual heat transfer coefficient for each core type once the optimum unit cell number was determined using the theoretical model.

Fig. 11(b) plotted the maximum rate of heat transfer that a specific core could achieve at the optimum unit cell number as a function of pumping power. Among the 5 core topologies (*i.e.*, I, V, N, W and M) with optimum unit cell numbers, the I core exhibited the highest rate of heat dissipation at a given pumping power, while the M core yielded the lowest rate. Therefore, in terms of overall thermal performance, the I core is the best topology among the five selected topologies.

Although the quadrilateral core (I core) had the best heat transfer performance, it was likely to buckle under small deformation when subjected to out-of-plane compression. On the contrary, the triangular core could convert certain compressive load into shear load, thus significantly improving its critical buckling load. For load bearing, therefore, the triangular core was superior to the quadrilateral core. The contradiction between heat transfer and load bearing makes it necessary to consider the balance of these two aspects in thermo-mechanical design of core structures. This issue will be addressed in a future study.

7. Conclusion

Lightweight sandwich-walled cylinders are ideal candidates for multifunctional applications such as simultaneous load bearing and active cooling. In the current study, the thermo-fluid performance of sandwich-walled cylinders with varying core morphologies was systematically investigated by experimental measurement, numerical simulation and theoretical modeling. The main results obtained were summarized as:

1 Comparing the numerical simulation results of both laminar and turbulent flow models with the experimental measurements revealed that, as the Reynolds number was increased, flow in the channels of the sandwich-walled cylinder changed from laminar ($Re < 2200$), transition ($2200 < Re < 4100$) to vigorous turbulence stage ($Re > 4100$). The results provide useful guidance for the selection of numerical models for different flow stages.
2 Subject to the constraint of identical heat dissipation area, the influence of pore morphology on heat transfer and flow resistance of sandwich-walled cylinder was quantified. Pore shape and pore distribution pattern played important roles in the heat dissipation capacity of the cylinder. For uniformly distributed pores, the heat transfer coefficient of quadrilateral cores was 5%–20% higher than triangular cores, at the expense of 10% higher of flow resistance in the laminar flow range. For the same triangular core, the non-homogeneity in pore structure did not affect flow resistance but caused a 10% drop in heat transfer coefficient.
3 Optimal unit cell number was obtained for each core type using the intersection-of-asymptotes theory. Corresponding maximal heat transfer coefficients for five different cores types were calculated by CFD and compared with each other to search for the best core design. Under the condition of fixed pumping power, the I core (quadrilateral core) exhibited the best overall heat transfer performance while the M core had the worst performance.

Declaration of Competing Interest

We wish to draw the attention of the Editor to the following facts which may be considered as potential conflicts of interest and to significant financial contributions to this work.

We confirm that the manuscript has been read and approved by all named authors and that there are no other persons who satisfied the criteria for authorship but are not listed. We further confirm that the order of authors listed in the manuscript has been approved by all of us.

We confirm that we have given due consideration to the protection of intellectual property associated with this work and that there are no impediments to publication, including the timing of publication, with respect to intellectual property. In so doing we confirm that we have followed the regulations of our institutions concerning intellectual property.

CRediT authorship contribution statement

Shanyouming Sun: Investigation, Software, Data curation, Validation, Formal analysis, Writing - original draft. **Shangsheng Feng:** Conceptualization, Methodology, Writing - review & editing, Funding acquisition. **Qiancheng Zhang:** Visualization. **Tian Jian Lu:** Supervision, Funding acquisition, Writing - review & editing.

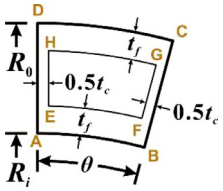

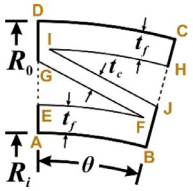

Acknowledgements

This work was supported by the National Natural Science Foundation of China (51676156 and 11972185), the National "111" Project of China (B06024), the Postdoctoral Science Foundation of China (2016M590942) and the Research Fund of State Key Laboratory of Mechanics and Control of Mechanical Structures (MCMS-E-0219K02 and MCMS-I-0219K01).

Appendix: Relations between geometric parameters of 5 core morphologies

1. I core

With the center of sandwich-walled cylinder taken as the origin of coordinates, a plane rectangular coordinate system was established. As a result, the horizontal and vertical coordinates of points A~F were:

$$x_A = 0, y_A = R_i \tag{54}$$

$$x_B = R_i \sin\theta, y_B = R_i \cos\theta \tag{55}$$

$$x_C = R_0 \sin\theta, y_C = R_0 \cos\theta \tag{56}$$

$$x_D = 0, y_D = R_0 \tag{57}$$

$$x_E = 0.5t_c, y_E = \sqrt{\left(R_i + t_f\right)^2 - (0.5t_c)^2} \tag{58}$$

$$x_F = -0.5t_c \cos\theta + \sin\theta\sqrt{\left(R_i + t_f\right)^2 - (0.5t_c)^2}, y_F = \frac{x_F}{\tan\theta} + \frac{0.5t_c}{\sin\theta} \tag{59}$$

$$x_G = -0.5t_c \cos\theta + \sin\theta\sqrt{\left(R_0 - t_f\right)^2 - (0.5t_c)^2}, y_G = \frac{x_G}{\tan\theta} + \frac{0.5t_c}{\sin\theta} \tag{60}$$

$$x_H = -0.5t_c, y_H = \sqrt{\left(R_0 - t_f\right)^2 - (0.5t_c)^2} \tag{61}$$

The area of the quadrilateral EFGH was:

$$S_{EFGH} = \int_{x_E}^{x_F}\left[\sqrt{\left(R_0 - t_f\right)^2 - x^2} - \sqrt{\left(R_i + t_f\right)^2 - x^2}\right]dx + \int_{x_F}^{x_G}\left[\sqrt{\left(R_0 - t_f\right)^2 - x^2} - \left(\frac{x}{\tan\theta} + \frac{0.5t_c}{\sin\theta}\right)\right]dx \tag{62}$$

The circumference of EFGH (*i.e.*, the wet circumference of flow channel) was:

$$C_{EFGH} = y_H - y_E + \sqrt{(x_G - x_F)^2 + (y_G - y_F)^2} + \left(R_i + t_f\right)\left(\arctan\frac{y_E}{x_E} - \arctan\frac{y_F}{x_F}\right) + \left(R_0 - t_f\right)\left(\arctan\frac{y_H}{x_H} - \arctan\frac{y_G}{x_G}\right) \tag{63}$$

The porosity ε_p was:

$$\varepsilon_p = \frac{2S_{EFGH}}{\left(R_0^2 - R_i^2\right)\theta} \tag{64}$$

The total heat dissipation area S_t satisfied:

$$S_t = C_{EFGH} L \tag{65}$$

The hydraulic diameter of the channel, D, satisfied:

$$D = \frac{4S_{EFGH}}{C_{EFGH}} \tag{66}$$

2. V core

The horizontal and vertical coordinates of points A~J as sketched above were:

$$x_A = 0, y_A = R_i \tag{67}$$

$$x_B = R_i \sin\theta, y_B = R_i \cos\theta \tag{68}$$

$$x_C = R_0 \sin\theta, y_C = R_0 \cos\theta \tag{69}$$

$$x_D = 0, y_D = R_0 \tag{70}$$

$$x_E = 0, y_E = R_i + t_f \tag{71}$$

$$x_F = -0.5t_c cos\theta + sin\theta\sqrt{\left(R_i + t_f\right)^2 - (0.5t_c)^2}, y_F = \frac{x_F}{\tan\theta} + \frac{0.5t_c}{\sin\theta} \tag{72}$$

$$x_G = 0, y_G = y_F - kx_F \tag{73}$$

$$x_H = \left(R_0 - t_f\right)\sin\theta, y_H = \frac{x_H}{\tan\theta} \tag{74}$$

$$x_I = 0.5t_c, y_I = \sqrt{\left(R_0 - t_f\right)^2 - (0.5t_c)^2} \tag{75}$$

$$x_J = \frac{(0.5kt_c - y_I)\sin\theta}{k\sin\theta - \cos\theta}, y_J = k\left(x_J - 0.5t_c\right) + y_I \tag{76}$$

(76)

where k satified:

$$k = \frac{-(y_I - y_F)(x_F - 0.5t_c) + t_c\sqrt{\left[(x_F - 0.5t_c)^2 + (y_I - y_F)^2\right] - t_c^2}}{(x_F - 0.5t_c)^2 - t_c^2} \tag{77}$$

The surface areas of the curved triangles EFG and HIJ were:

$$S_{EFG} = \int_0^{x_F}\left[k(x - x_F) + y_F - \sqrt{\left(R_i + t_f\right)^2 - x^2}\right]dx \tag{78}$$

$$S_{HIJ} = \int_{0.5t_c}^{x_J}\left\{\sqrt{\left(R_0 - t_f\right)^2 - x^2} - [k(x - 0.5t_c) + y_I]\right\}dx + \int_{x_J}^{x_H}\left[\sqrt{\left(R_0 - t_f\right)^2 - x^2} - \frac{x}{\tan\theta}\right]dx \tag{79}$$

The total length of straight edges GF, IJ as well as arc edges EF and IH was calculated as:

$$C_{GF,IJ,\widehat{EF},\widehat{IH}} = \sqrt{(x_G - x_F)^2 + (y_G - y_F)^2} + \sqrt{\left(x_I - x_J\right)^2 + \left(y_I - y_J\right)^2}$$

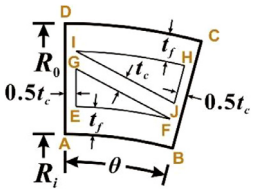

$$+\left(R_i+t_f\right)\left(\arctan\frac{y_E}{x_E}-\arctan\frac{y_F}{x_F}\right)$$
$$+\left(R_0-t_f\right)\left(\arctan\frac{y_I}{x_I}-\arctan\frac{y_H}{x_H}\right) \quad (80)$$

The porosity ε_p was:

$$\varepsilon_p=\frac{2\left(S_{EFG}+S_{HIJ}\right)}{\left(R_0^2-R_i^2\right)\theta} \quad (81)$$

The total heat dissipation area S_t satisfied:

$$S_t=C_{GF,IJ,\widehat{EF},\widehat{IH}}\cdot L \quad (82)$$

The hydraulic diameter D satisfied:

$$D=\frac{4\left(S_{EFG}+S_{HIJ}\right)}{C_{GF,IJ,\widehat{EF},\widehat{IH}}} \quad (83)$$

3. N core

The horizontal and vertical coordinates of points A~J were:

$$x_A=0, y_A=R_i \quad (84)$$

$$x_B=R_i\sin\theta, y_B=R_i\cos\theta \quad (85)$$

$$x_C=R_0\sin\theta, y_C=R_0\cos\theta \quad (86)$$

$$x_D=0, y_D=R_0 \quad (87)$$

$$x_E=0.5t_c, y_E=\sqrt{\left(R_i+t_f\right)^2-(0.5t_c)^2} \quad (88)$$

$$x_F=-0.5t_c cos\theta+sin\theta\sqrt{\left(R_i+t_f\right)^2-(0.5t_c)^2}, y_F=\frac{x_F}{\tan\theta}+\frac{0.5t_c}{\sin\theta} \quad (89)$$

$$x_G=0.5t_c, y_G=k(0.5t_c-x_F)+y_F \quad (90)$$

$$x_H=-0.5t_c\cos\theta+\sin\theta\sqrt{\left(R_0-t_f\right)^2-(0.5t_c)^2}, y_H=\frac{x_H}{\tan\theta}+\frac{0.5t_c}{\sin\theta} \quad (91)$$

$$x_I=0.5t_c, y_I=\sqrt{\left(R_0-t_f\right)^2-(0.5t_c)^2} \quad (92)$$

$$x_J=\frac{0.5t_c+(0.5kt_c-y_I)\sin\theta}{k\sin\theta-\cos\theta}, y_J=k\left(x_J-0.5t_c\right)+y_I \quad (93)$$

The coefficient k satisfied Eq. (76). The surface areas of curved triangles EFG and HIJ were:

$$S_{EFG}=\int_{0.5t_c}^{x_F}\left[k(x-x_F)+y_F-\sqrt{\left(R_i+t_f\right)^2-x^2}\right]dx \quad (94)$$

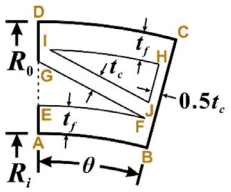

$$S_{HIJ}=\int_{0.5t_c}^{x_J}\left\{\sqrt{\left(R_0-t_f\right)^2-x^2}-[k(x-0.5t_c)+y_I]\right\}dx$$
$$+\int_{x_J}^{x_H}\left[\sqrt{\left(R_0-t_f\right)^2-x^2}-\left(\frac{x}{\tan\theta}+\frac{0.5t_c}{\sin\theta}\right)\right]dx \quad (95)$$

The circumferences of curved triangles EFG and HIJ (*i.e.*, wet circumferences of channels) were given by:

$$C_{EFG}=y_G-y_E+\sqrt{(x_G-x_F)^2+(y_G-y_F)^2}$$
$$+\left(R_i+t_f\right)\left(\arctan\frac{y_E}{x_E}-\arctan\frac{y_F}{x_F}\right) \quad (96)$$

$$C_{HIJ}=\sqrt{\left(x_I-x_J\right)^2+\left(y_I-y_J\right)^2}+\sqrt{\left(x_H-x_J\right)^2+\left(y_H-y_J\right)^2}$$
$$+\left(R_0-t_f\right)\left(\arctan\frac{y_I}{x_I}-\arctan\frac{y_H}{x_H}\right) \quad (97)$$

The porosity was:

$$\varepsilon_p=\frac{2\left(S_{EFG}+S_{HIJ}\right)}{\left(R_0^2-R_i^2\right)\theta} \quad (98)$$

The total heat dissipation area was:

$$S_t=\left(C_{EFG}+C_{HIJ}\right)L \quad (99)$$

and the hydraulic diameter was:

$$D=\frac{4\left(S_{EFG}+S_{HIJ}\right)}{C_{EFG}+C_{HIJ}} \quad (100)$$

4. W core

The horizontal and vertical coordinates of points A~J were:

$$x_A=0, y_A=R_i \quad (101)$$

$$x_B=R_i\sin\theta, y_B=R_i\cos\theta \quad (102)$$

$$x_C=R_0\sin\theta, y_C=R_0\cos\theta \quad (103)$$

$$x_D=0, y_D=R_0 \quad (104)$$

$$x_E=0, y_E=R_i+t_f \quad (105)$$

$$x_F=-0.5t_c cos\theta+sin\theta\sqrt{\left(R_i+t_f\right)^2-(0.5t_c)^2}, y_F=\frac{x_F}{\tan\theta}+\frac{0.5t_c}{\sin\theta} \quad (106)$$

$$x_G=0, y_G=y_F-kx_F \quad (107)$$

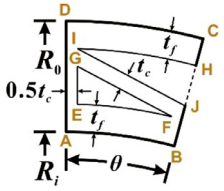

$$x_H = -0.5t_c\cos\theta + \sin\theta\sqrt{(R_0 - t_f)^2 - (0.5t_c)^2},\ y_H = \frac{x_H}{\tan\theta} + \frac{0.5t_c}{\sin\theta} \tag{108}$$

$$x_I = 0.5t_c,\ y_I = \sqrt{(R_0 - t_f)^2 - (0.5t_c)^2} \tag{109}$$

$$x_J = \frac{0.5t_c + (0.5kt_c - y_I)\sin\theta}{k\sin\theta - \cos\theta},\ y_J = k(x_J - 0.5t_c) + y_I \tag{110}$$

The coefficient k satisfied Eq. (76). The surface areas of curved triangles EFG and HIJ were:

$$S_{EFG} = \int_0^{x_F}\left[k(x - x_F) + y_F - \sqrt{(R_i + t_f)^2 - x^2}\right]dx \tag{111}$$

$$S_{HIJ} = \int_{0.5t_c}^{x_J}\left\{\sqrt{(R_0 - t_f)^2 - x^2} - [k(x - 0.5t_c) + y_I]\right\}dx + \int_{x_J}^{x_H}\left[\sqrt{(R_0 - t_f)^2 - x^2} - \left(\frac{x}{\tan\theta} + \frac{0.5t_c}{\sin\theta}\right)\right]dx \tag{112}$$

The length of straight edge GF, arc edge EF and the circumference of curved triangle HIJ were calculated as:

$$C_{GF,\widehat{EF}} = \sqrt{(x_G - x_F)^2 + (y_G - y_F)^2} + (R_i + t_f)\left(\arctan\frac{y_E}{x_E} - \arctan\frac{y_F}{x_F}\right) \tag{113}$$

$$C_{HIJ} = \sqrt{(x_I - x_J)^2 + (y_I - y_J)^2} + \sqrt{(x_H - x_J)^2 + (y_H - y_J)^2} + (R_0 - t_f)\left(\arctan\frac{y_I}{x_I} - \arctan\frac{y_H}{x_H}\right) \tag{114}$$

The porosity was:

$$\varepsilon_p = \frac{2(S_{EFG} + S_{HIJ})}{(R_0^2 - R_i^2)\theta} \tag{115}$$

The total heat dissipation area was:

$$S_t = \left(C_{GF,\widehat{EF}} + C_{HIJ}\right)L \tag{116}$$

The hydraulic diameter was:

$$D = \frac{4(S_{EFG} + S_{HIJ})}{C_{GF,\widehat{EF}} + C_{HIJ}} \tag{117}$$

5. M core

The horizontal and vertical coordinates of points A~J were:

$$x_A = 0,\ y_A = R_i \tag{118}$$

$$x_B = R_i\sin\theta,\ y_B = R_i\cos\theta \tag{119}$$

$$x_C = R_0\sin\theta,\ y_C = R_0\cos\theta \tag{120}$$

$$x_D = 0,\ y_D = R_0 \tag{121}$$

$$x_E = 0.5t_c,\ y_E = \sqrt{(R_i + t_f)^2 - (0.5t_c)^2} \tag{122}$$

$$x_F = -0.5t_c cos\theta + sin\theta\sqrt{(R_i + t_f)^2 - (0.5t_c)^2},\ y_F = \frac{x_F}{\tan\theta} + \frac{0.5t_c}{\sin\theta} \tag{123}$$

$$x_G = 0.5t_c,\ y_G = k(0.5t_c - x_F) + y_F \tag{124}$$

$$x_H = (R_0 - t_f)\sin\theta,\ y_H = \frac{x_H}{\tan\theta} \tag{125}$$

$$x_I = 0.5t_c,\ y_I = \sqrt{(R_0 - t_f)^2 - (0.5t_c)^2} \tag{126}$$

$$x_J = \frac{(0.5kt_c - y_I)\sin\theta}{k\sin\theta - \cos\theta},\ y_J = k(x_J - 0.5t_c) + y_I \tag{127}$$

The coefficient k satisfied Eq. (76). The surface areas of curved triangles EFG and HIJ were:

$$S_{EFG} = \int_{0.5t_c}^{x_F}\left[k(x - x_F) + y_F - \sqrt{(R_i + t_f)^2 - x^2}\right]dx \tag{128}$$

$$S_{HIJ} = \int_{0.5t_c}^{x_J}\left\{\sqrt{(R_0 - t_f)^2 - x^2} - [k(x - 0.5t_c) + y_I]\right\}dx + \int_{x_J}^{x_H}\left[\sqrt{(R_0 - t_f)^2 - x^2} - \frac{x}{\tan\theta}\right]dx \tag{129}$$

The circumference of curved triangle EFG and the total length of straight edge IJ and arc edge IH were given by:

$$C_{EFG} = y_G - y_E + \sqrt{(x_G - x_F)^2 + (y_G - y_F)^2} + (R_i + t_f)\left(\arctan\frac{y_E}{x_E} - \arctan\frac{y_F}{x_F}\right) \tag{130}$$

$$C_{IJ,\widehat{IH}} = \sqrt{(x_I - x_J)^2 + (y_I - y_J)^2} + (R_0 - t_f)\left(\arctan\frac{y_I}{x_I} - \arctan\frac{y_H}{x_H}\right) \tag{131}$$

The porosity was:

$$\varepsilon_p = \frac{2(S_{EFG} + S_{HIJ})}{(R_0^2 - R_i^2)\theta} \tag{132}$$

The total heat dissipation area was:

$$S_t = \left(C_{EFG} + C_{IJ,\widehat{IH}}\right)L \tag{133}$$

and the hydraulic diameter was:

$$D = \frac{4(S_{EFG} + S_{HIJ})}{C_{EFG} + C_{IJ,\widehat{IH}}} \tag{134}$$

References

[1] L. Valdevit, N. Vermaak, F.W. Zok, et al., A materials selection protocol for lightweight actively cooled panels, J. Appl. Mech. 75 (6) (2008) 061022.
[2] A.M Mellor, Design of Modern Combustors I, Academic Press, 1991.
[3] G. Xie, C. Wang, T. Ji, et al., Investigation on thermal and thermomechanical performances of actively cooled corrugated sandwich structures, Appl. Therm. Eng. 103 (2016) 660–669.
[4] C. Shu, S Hou, Theoretical prediction on corrugated sandwich panels under bending loads, Acta Mech. Sin. 34 (5) (2018) 925–935.
[5] T. Liu, Z.C. Deng, T.J Lu, Bi-functional optimization of actively cooled, pressurized hollow sandwich-walled cylinders with prismatic cores, J. Mech. Phys. Solids 55 (2007) 2565–2602.
[6] Q.C. Zhang, X.H. Yang, P. Li, et al., Bioinspired engineering of honeycomb structure - using nature to inspire human innovation, Prog. Mater Sci. 74 (2015) 332–400.
[7] S.V. Murphy, A Atala, 3D bioprinting of tissues and organs, Nat. Biotechnol. 32 (2014) 773–785.
[8] B Han, Mechanical Behaviors of Reinforced Corrugated Composite Cellular Materials, Xi'an Jiaotong University, Xi'an, 2015.
[9] P.B. Su, B. Han, M. Yang, et al., Axial compressive collapse of ultralight corrugated sandwich cylindrical shells, Mater. Des. 160 (2018) 325–337.
[10] F. Cote, V.S. Deshpande, N.A. Fleck, et al., The compressive and shear responses of corrugated and diamond lattice materials, Int. J. Solids Struct. 43 (20) (2006) 6220–6242.
[11] Wevers L.J., Vredeveldt A.W. Full scale ship collision experiments 1998. TNO-report 98-CMC-R1725, The Netherlands; 1999.
[12] V. Rubino, V.S. Deshpande, N.A Fleck, The three-point bending of y-frame and corrugated core sandwich beams, Int. J. Mech. Sci. 52 (3) (2010) 485–494.
[13] T.J Lu, Heat transfer efficiency of metal honeycombs, Int. J. Heat Mass Transf. 42 (11) (1997) 2031–2040.
[14] C.Y. Zhao, T.J Lu, Analysis of microchannel heat sinks for electronics cooling, Int. J. Heat Mass Transf. 45 (24) (2002) 4857–4869.
[15] B Zohuri, Compact Heat Exchangers, Springer, Switzerland, 2017.
[16] T. Wen, F. Xu, T.J Lu, Structural optimization of two-dimensional cellular metals cooled by forced convection, Int. J. Heat Mass Transf. 50 (2007) 2590–2604.
[17] Q.W. Wang, M. Lin, M Zeng, Effect of lateral fin profiles on turbulent flow and heat transfer performance of internally finned tubes, Appl. Therm. Eng. 29 (2009) 3006–3013.
[18] A Bejan, Convection Heat Transfer, 2nd Edition, John Wiley & Sons Inc., New Jersey, 1995.
[19] Y. Chen, Y. Wang, Z. Bao, et al., Numerical investigation of flow distribution and heat transfer of hydrocarbon fuel in regenerative cooling panel, Appl. Therm. Eng. 98 (2016) 628–635.
[20] T. Jing, G. He, W. Li, et al., Flow and thermal analyses of regenerative cooling in non-uniform channels for combustion chamber, Appl. Therm. Eng. 119 (2017) 89–97.
[21] G.P. Sutton, O Biblarz, Rocket Propulsion Elements, 9th Edition, John Wiley & Sons Inc., New Jersey, 2017.
[22] J. Song, B Sun, Coupled numerical simulation of combustion and regenerative cooling in LOX/Methane rocket engines, Appl. Therm. Eng. 106 (2016) 762–773.
[23] I. Dayyani, A.D. Shaw, F.E.I. Saavedra, et al., The mechanics of composite corrugated structures: a review with applications in morphing aircraft, Compos. Struct. 133 (2015) 358–380.
[24] W. Qu, I Mudawar, Experimental and numerical study of pressure drop and heat transfer in a single-phase micro-channel heat sink, Int. J. Heat Mass Transf. 45 (12) (2002) 2549–2565.
[25] M.M. Ali, S Ramadhyani, Experiments on convective heat transfer in corrugated channels, Exp. Heat Transf. 5 (1992) 175–193.
[26] S.S. Feng, F. Li, F. Zhang, et al., Natural convection in metal foam heat sinks with open slots, Exp. Therm. Fluid Sci. 91 (2018) 354–362.
[27] S.S. Feng, M. Shi, H. Yan, et al., Natural convection in a cross-fin heat sink, Appl. Therm. Eng. 132 (2018) 30–37.
[28] H.W. Coleman, W.G Steele, Experimentation and Uncertainty Analysis For Engineers, 2nd Edition, John Wiley & Sons Inc., New Jersey, 1999.
[29] E. Eckert, T Irvine, Pressure drop and heat transfer in a duct with triangular cross-section, ASME J. Heat Transf. 83 (1960) 125–136.
[30] B. Yu, W.Q Tao, Pressure drop and heat transfer characteristics of turbulent flow in annular tubes with internal wave-like longitudinal fins, Heat Mass Transf. 40 (2004) 643–651.
[31] ANSYS FLUENT, 14.5 User's & Tutorial Guide, ANSYS Inc., Canonsburg, PA, 2012.
[32] S.S. Feng, S. Sun, H. Yan, et al., Optimum composition of gas mixture in a novel chimney-based led bulb, Int. J. Heat Mass Transf. 115 (2017) 32–42.
[33] S.S. Feng, M. Shi, Y.F. Li, et al., Pore-scale and volume-averaged numerical simulations of melting phase change heat transfer in finned metal foam, Int. J. Heat Mass Transf. 90 (2015) 838–847.
[34] S.S. Feng, J.J. Kuang, T. Wen, et al., An experimental and numerical study of finned metal foam heat sinks under impinging air jet cooling, Int. J. Heat Mass Transf. 77 (2014) 1063–1074.
[35] R.K. Shah, A.L London, Laminar Flow Forced Convection in ducts: a Source Book For Compact Heat Exchanger Analytical Data, Academic Press, New York, 1978.
[36] L.W. Carlson, T.F Irvine, Fully developed pressure drop in triangular shaped ducts, ASME J. Heat Transf. 83 (4) (1964) 441–444.